Advances in Water Resources 162 (2022) 104152

Contents lists available at ScienceDirect

Advances in Water Resources

journal homepage: www.elsevier.com/locate/advwatres

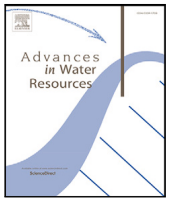

A pore-resolved interface tracking algorithm for simulating multiphase flow in arbitrarily structured porous media

Zhongzheng Wang [a,b,c], Jean-Michel Pereira [c], Emilie Sauret [a], Saman A. Aryana [d], Zhang Shi [b,e], Yixiang Gan [b,f,*]

[a] School of Mechanical, Medical and Process Engineering, Faculty of Engineering, Queensland University of Technology, QLD 4001, Australia
[b] School of Civil Engineering, The University of Sydney, NSW 2006, Australia
[c] Navier, Ecole des Ponts, Univ Gustave Eiffel, CNRS, Marne-la-Vallée, France
[d] Department of Chemical Engineering, University of Wyoming, Laramie, WY 82071, USA
[e] School of Mechanical and Mining Engineering, The University of Queensland, QLD 4072, Australia
[f] The University of Sydney Nano Institute (Sydney Nano), The University of Sydney, NSW 2006, Australia

ARTICLE INFO

Keywords:
Multiphase flow
Interface tracking algorithm
Pore-network model
Wettability
Porous media

ABSTRACT

We present an interface tracking algorithm that incorporates essential pore-scale invasion mechanisms for simulating multiphase flow in porous media in capillary dominated regime. The algorithm allows the capture of the actual shape of porous medium with complex geometrical features, including both convex and concave particles or irregular channels. It also incorporates the sharp edge pinning effect such that pinning of menisci at corners can be naturally taken into account. We firstly conduct simulations under imbibition and drainage conditions in a single junction micro-model and in disordered porous media for validation. It is shown that the invasion mechanisms at pore scale are accurately captured, and the macroscopic invasion morphology in porous media are reproduced. A series of simulations for fluid displacement processes are carried out across a wide range of intrinsic contact angles in a two-dimensional representation of a Berea sandstone. The transition between stable displacement and capillary fingering is characterized using displacement efficiency, fractal dimension, and fluid–fluid interfacial length. This work deepens the understanding of fluid–fluid displacement processes in porous media. Furthermore, the presented interface tracking algorithm offers a highly efficient tool for further exploration of effects of wettability, geometry, and topology on multiphase flow in realistic porous materials.

1. Introduction

The phenomenon where one fluid displaces another in porous materials is ubiquitous in many natural and industrial processes, such as water infiltration into soils (Lipiec et al., 2006), hydrogen fuel cells (Bao and Gan, 2020), enhanced oil recovery (Lake et al., 2014; Blunt et al., 1993), and carbon geological sequestration (Szulczewski et al., 2012; Matter et al., 2016). Understanding the mechanisms of multiphase flow in porous media is of vital importance for prediction and control of fluid transport in various engineering problems. It has been established that the pattern formation of fluid–fluid displacement depends on both fluid properties and flow conditions (Lenormand et al., 1988; Lenormand, 1990; Yortsos et al., 1997; Armstrong et al., 2014; Holtzman, 2016; Ju et al., 2020), which can be described by the Capillary number, reflecting the relative importance of viscous forces to capillary forces, and viscosity ratio. Depending on the viscosity of fluids, interfacial tension, and injection velocity, different invasion morphologies including capillary fingering, viscous fingering, and stable displacement have been observed numerically and experimentally, both in 2D microfluidics (e.g., Hele-Shaw cells) and 3D granular materials (Lenormand, 1990; Trojer et al., 2015; Zhao et al., 2016; Guo and Aryana, 2019; Singh et al., 2017; An et al., 2020; Patmonoaji et al., 2020). At the same time, the wetting condition of the solid skeleton, characterized by the contact angle formed at the fluid–fluid–solid triple line, can also greatly impact the pattern formation during the fluid–fluid displacement processes (Crisp and Thorpe, 1948; Purcell, 1950; Mason and Morrow, 1994; Cieplak and Robbins, 1990; Trojer et al., 2015; Jung et al., 2016; Wang et al., 2019, 2020; Shi et al., 2021; Holtzman and Segre, 2015; Zhao et al., 2016; Ran et al., 2018; Primkulov et al., 2018; Wang et al., 2021). Specifically, when the solid shifts from non-wetting (drainage, contact angle $\theta > 90°$) to wetting (imbibition, $\theta < 90°$) to the invading fluid, the invasion front

* Corresponding author.
E-mail address: yixiang.gan@sydney.edu.au (Y. Gan).

https://doi.org/10.1016/j.advwatres.2022.104152
Received 25 October 2021; Received in revised form 9 January 2022; Accepted 12 February 2022
Available online 26 February 2022

is smoothed, corresponding to the transition from viscous/capillary fingering towards compact displacement.

Pore-network models have been extensively applied to study multiphase flow in porous media due to their favorable computational cost compared with conventional computational methods, i.e., Navier Stokes solvers (Blunt, 1998, 2001; Cieplak and Robbins, 1988, 1990; Holtzman and Segre, 2015; Holtzman, 2016; Primkulov et al., 2018; Hu et al., 2019; Wang et al., 2021). Pore-network model are rigorous tools for reproducing macroscopic invasion morphologies, and consequently revealing potential connections between pore-scale mechanisms and macroscopic observations. In the seminal work by Cieplak and Robbins (1988, 1990), an interface-tracking algorithm considering different pore-filling events was shown to capture the transition from capillary fingering to compact displacement. The *overlap* event, during which two menisci merge and form a new meniscus, is found to be the key mechanism that smooths the invasion front and suppresses trapping of defending phase, leading to an overall more stable displacement. The interface-tracking algorithm originated from the work by Cieplak and Robbins (1988, 1990) has been adopted, or extended, to study the impact of wettability, viscosity, disorder, and corner flows during fluid–fluid displacement processes (Holtzman and Segre, 2015; Primkulov et al., 2018, 2019; Hu et al., 2019). For example, by adding the dynamic effect, from the pore-network simulation results across a wide range of capillary numbers, the likelihood of the overlap event is found to strongly correlate with total fluid–fluid interfacial area and finger width (Holtzman and Segre, 2015).

However, one limitation of the aforementioned pore-network models is that they are only applicable to porous media composed of perfectly spherical grains, whereas in most natural systems such as sand packs and surrogate models such as microfluidics, solid surface with irregular shape or sharp edges are often encountered. Due to these non-smooth surfaces, pinning of menisci during displacement process may be observed (Gibbs, 1961; Oliver et al., 1977), which leads to effective contact angles deviating from the intrinsic one, altering the capillary pressure resistance at local pore/throat. The sharp edge pinning phenomenon has also been studied by Wu et al. (2016) (termed "capillary valve effect"). It was demonstrated that the pinning of meniscus needs to be considered in order to obtain accurate details of two-phase flows, especially during imbibition processes. Recently, an extended pore-network model (EPONM) with consideration of particle shape was proposed to investigate immiscible two-phase flows in the capillary dominated regime (Wang et al., 2021). It is shown that the presence of sharp corners, and the subsequent meniscus pinning, leads to an effective contact angle that deviates from the intrinsic one. Nevertheless, only particles represented by simple polygons arranged on a regular triangular lattice are considered (Wang et al., 2021).

In this work, we further extend the interface tracking algorithm for multiphase flow, making it applicable to porous media of arbitrary pore structures and grain shapes such as reconstructed pore geometries from 2D scans of rock samples. We first present the algorithm along with an explanation of the physical mechanisms that are captured by the method. This is followed by simulations of two-phase flow in single junction micro-models and disordered porous media for validation purpose. Then, to demonstrate the capability of the algorithm, we carry out systematic simulations in representative porous media that are constructed based on a Berea sandstone across a wide range of contact angles. We analyze the effects of wettability on multiphase flow in this realistic porous medium by focusing on a few important metrics that are often used to characterize the displacement patterns, including sweep efficiency, fractal dimension, and fluid–fluid interfacial area.

2. Methods

For a given two-dimensional porous medium represented in a grayscale image, the grain boundary surfaces are detected and discretized into computational nodes (i.e., black dots in Fig. 1(D)) according to a prescribed mesh size. This is followed by the initialization of a set of arcs with radius r representing the menisci (fluid–fluid interfaces). The initial value of r is chosen according to the local pore geometry and the effective contact angle θ, where the effective contact angle is the angle measured within the invading phase at the triple contact point, which is equal to the intrinsic contact angle θ_0 at perfectly smooth surface, and could be larger than θ_0 at sharp corners [Fig. 1(A)] due to the sharp edge pinning effect as we will discuss later. For every meniscus, different potential advancement events are considered. Here, we consider (i) a *burst* event, corresponding to the capillary pressure associated with meniscus shape indicated by the blue-dashed lines in Fig. 1(B); (ii) a *touch* event, corresponding to the capillary pressure associated with meniscus shape indicated by the blue-solid lines in Fig. 1(B); and (iii) an *unpin* event (for both left and right triple points), corresponding to the capillary pressure when the effective contact angle reaches the unpin angle $\theta_{\text{unpin}} = \theta_0 + (180° - \alpha)$ [Fig. 1(A)]. This is to capture the sharp edge pinning phenomenon where the equilibrium state of effective contact angle θ cannot exceed θ_{unpin} according to a purely geometrical extension of Young–Dupre equation (Gibbs, 1961; Oliver et al., 1977).

Fig. 2(A-B) shows in more detail the determination of meniscus advancement events. In Fig. 2(A), the circle associated with the *unpin* event at the right triple point (with the invading direction as the frame of reference, i.e., black arrow) is shown in orange, and the circle associated with the left triple-contact point are shown in purple. In this scenario, as the pressure within the invading fluid builds up and the meniscus bends forward, the *unpin* event at the right triple point (in orange) occurs first. In Fig. 2(B), the blue-solid and green-solid curves represent the menisci shapes for a *touch* and a *burst* event, respectively. The red box denotes the search box with red dots inside be considered as potential targets for the *touch* event. The purple square is determined to be the target *touch* point that makes the largest angle with two triple points. Note that the size of the search box should be greater than the largest pore size of the porous medium. For the *burst* event, the meniscus (green-solid curve) is a semicircle that corresponds to the smallest circle (largest pressure) for the given triple points. In this case, the *touch* event occurs before the *burst* event. The critical advancement pressure P_c for different events is calculated according to $P_c = \gamma/r$, with γ the interfacial tension and r the meniscus radius. The final P_c is chosen according to the event that occurs first (not necessarily the one with greatest/smallest P_c values). For the meniscus in Fig. 2(A-B), the final P_c is the one associated with the *unpin* event at the right triple point. Note that, if the middle grain in Fig. 2(B) was absent, the corresponding shape for a *touch* event would be represented by the blue-dashed curve. This *touch* event clearly takes place after the *burst* event, i.e., a post-burst event, and the P_c associated with this event is thus overwritten by the *burst* pressure (the meniscus has to reach burst state before finally touching the grain).

After updating the critical capillary pressure at each computational step, the meniscus with minimum P_c advances. The determination of the critical capillary pressure P_c for a given meniscus considering different types of instability events is based on the instability event that occurs first based on the local pore geometry and contact angle, regardless of the value of P_c. Globally, however, the meniscus with the smallest resistance (based on P_c value) advances. After each advancement, (iv) trapping of the defending phase is examined [Fig. 2(C)] and (v) an *overlap* event is checked and executed [Fig. 1(C)]. For a meniscus after an advancement. The trapping of the defending phase is checked by initializing a search path from the left triple point. The path follows the dry nodes [gray dots in Fig. 1(C)] in the clockwise direction, jumps to the left triple point once it reaches a right triple point, and stops when it reaches the outlet. A region is labeled trapped if the path returns to the starting point. Menisci 1 and 2 in Fig. 2(C) show a trapped and an active meniscus, respectively. Once a trapping event occurs, all menisci associated with the trapped region are deactivated to prevent further movement.

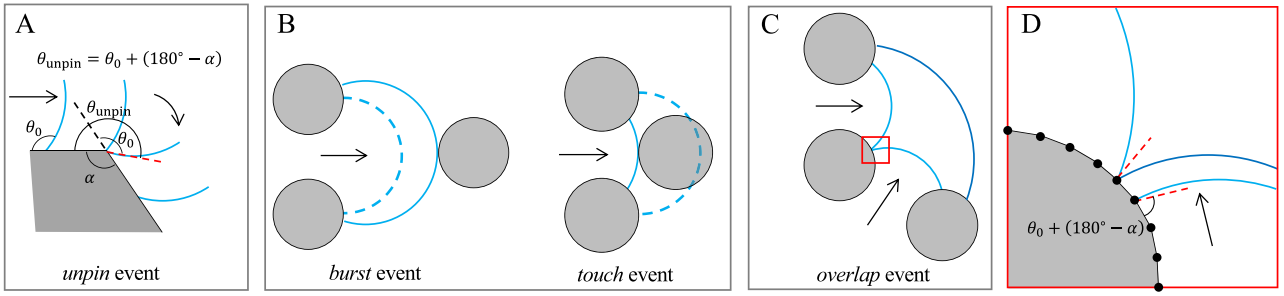

Fig. 1. Mechanisms of menisci advancement. (A) Meniscus with intrinsic contact angle θ_0 gets pinned at the sharp corner with the corner angle α. The meniscus adjusts shape without contact line movement until reaching an upper limit at θ_{unpin}, then it continues to advance. (B) A *burst* event (left) and *touch* event (right). The blue-dashed line marks the meniscus shape associated with the maximum capillary pressure resistance. Menisci number increases by one after *burst* or *touch*. (C) An *overlap* event, during which two menisci (light blue) merge into one (dark blue). (D) A local snapshot of (C). The bottom meniscus reaches its critical unpin contact angle marked by red-dashed lines, moving upward (from light blue to dark blue) to the next computational node (black dots) after which an *overlap* event is detected and executed.

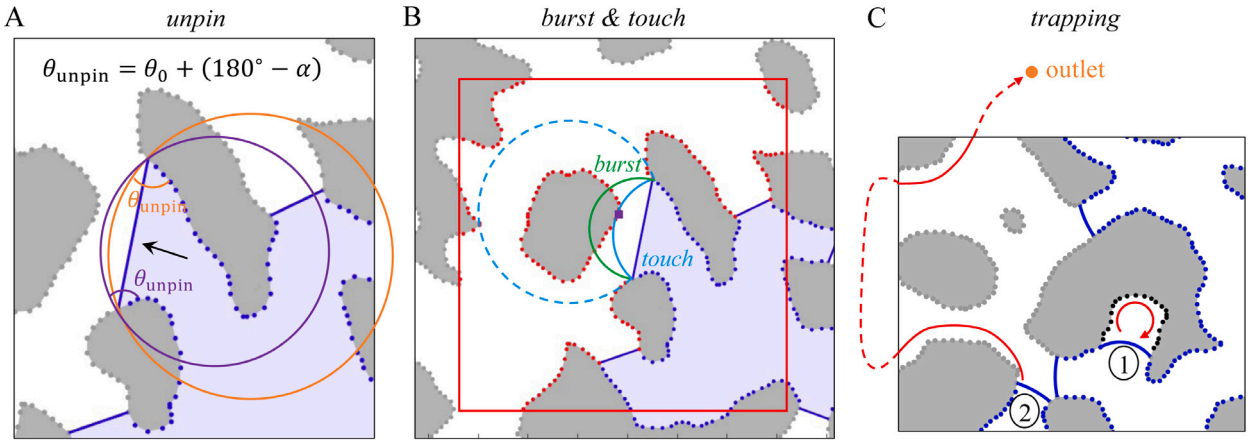

Fig. 2. Schematic showing the determination of advancement events. (A) The orange and purple circles are associated with the menisci shapes for *unpin* events at the right (with the invading direction as the frame of reference, i.e., black arrow) and left triple-contact points, respectively. (B) The blue-solid and green-solid curves are associated with the menisci shape for a *touch* and a *burst* event, respectively. The red rectangle is the search box, with all computation nodes in red color being considered as potential targets for the *touch* event, and the point marked by purple square is determined as the target *touch* point, which makes the largest angle with two triple points. In the case where the middle grain is absent, the meniscus shape for a *touch* event is marked by the blue-dashed line. (C) To determine whether a region is trapped after the advancement of a meniscus, a searching path following the clockwise direction is initialized from the left triple point. The search path follows dry nodes, jumps to the left triple point when reaching a right triple point, and stops when reaching the outlet. A region is labeled trapped if the path returns to the starting point. Menisci 1 and 2 show a trapped and an active meniscus, respectively.

Fig. 3(A) shows the flow chart of the algorithm. A sub-region of the grayscale image of a representation of a Berea sandstone (Guo and Aryana, 2019), and the corresponding snapshot of local menisci configuration during fluid displacement simulation, are shown in Fig. 3(B) and Fig. 3(C), respectively. Specifically, the gray, blue, and black dots represent dry, wetted, and trapped surfaces, respectively. Since the algorithm is based on discretization of pore space (more specifically, discrete grain boundaries) into computational nodes with a certain mesh size, it is necessary to conduct a mesh refinement study. As the menisci advancement is fundamentally governed by the determined capillary pressures associated with different invasion modes, as a rule of thumb, the mesh size, i.e., the distance between adjacent nodes, should be much smaller than the grain size and local throat size. For simulations in this work, the mesh refinement test is conducted, and it is found that having, on average, more than 25 nodes per grain for the porous media in Fig. 4(B) and more than 50 nodes per grain for porous medium in Fig. 5(A) are sufficient, and a further increase in the number of nodes per grain does not lead to a significant change in the results.

There are two major differences between the current algorithm and the interface tracking algorithm (and its derivatives) originally proposed by Cieplak and Robbins (1988, 1990). Firstly, the advancement of menisci in the current algorithm consists of a node-to-node movement, whereas the original one involves a pore-by-pore movement. The advantage of a node-to-node movement is its ability to capture the actual shape of a porous medium with complex geometrical features, including both convex and concave particles and irregular channels, whereas the original method is only applicable to porous media composed of perfect circular grains. Secondly, the sharp edge pinning effect is implemented such that pinning of the meniscus at corners can be naturally captured. This method provides a rigorous tool for studying two-phase flow in porous media, especially for investigating the combined impacts of topology, geometry, and wettability.

To validate the algorithm, we first conduct fluid displacement simulation in a single square junction under both drainage ($\theta_0 = 150°$) and imbibition ($\theta_0 = 60°$) conditions. This junction has a square pore body with edge length of unity, which is connected to four throats with widths of 0.1, 0.2, 0.3, and 0.4 on the top, right, bottom and left sides, respectively. For imbibition, to consider different pore filling mechanisms as in Lenormand et al. (1983), Lenormand and Zarcone (1984), three types of boundary conditions are considered (Fig. 4(A)) with the number of inlets ranging from one to three. We also conduct simulations of multiphase flow in disordered porous media and compare the results with those from the literature (Hu et al., 2019). The domain is filled with circular particles of different radii placed on a triangular lattice, and the fluid is injected from the left boundary with top and bottom boundaries treated as impermeable walls (Fig. 4(B)). The simulations stop when the invading phase reaches the outlet (the right boundary).

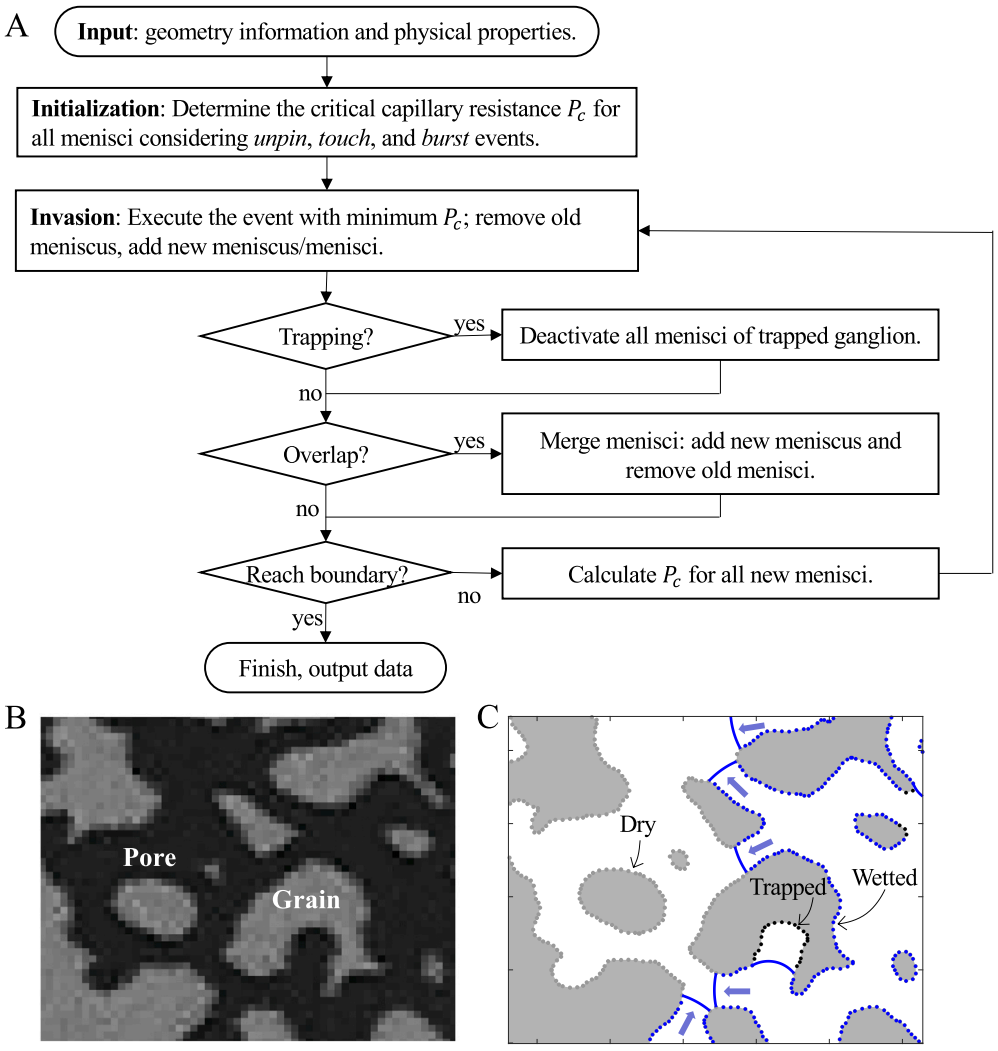

Fig. 3. Details on the interface tracking algorithm. (A) Flow chart of the algorithm. (B) A sub-region of grayscale image of a representation of a Berea sandstone (Guo and Aryana, 2019). Grains and pore space are in gray and black colors, respectively. (C) A snapshot of local menisci configuration during simulation. Dots denote the computational nodes. Specifically, gray, blue, and black colors represent dry, wetted, and trapped surfaces, respectively. Blue curves show the location of menisci. Blue arrows mark the menisci advancement directions..

To demonstrate the capability of the algorithm, we use the realistic porous medium described in Guo and Aryana (2019), which is shown in Fig. 5(A). The network represents the distribution of pores and throats observed in a thin section of Berea sandstone, and the detailed procedure is described in Alaskar (2013). Here, we consider a geometry relevant to oil recovery processes: a point inlet at the bottom-right corner as the injection well and a point outlet at the top-left corner as the withdrawal well (similar to Paterson (1984)). Again, the simulations stop when the invading phase reaches the outlet. For multi-phase flow with extreme wetting condition where the intrinsic contact angle is smaller than 45°, the corner flow phenomenon may start to appear (Zhao et al., 2016; Primkulov et al., 2018), allowing invading fluid to propagate without filling the pore bodies. This mechanism is currently not captured in the algorithm and we thus limit our attention to displacement processes under normal imbibition to strong drainage, i.e, intrinsic contact angles $\theta_0 \in [45°, 180°]$ at 5° increments. It is worth noting that recent experimental observations in microfluidic systems show that the critical intrinsic contact angle that marks the emergence of corner flow can be different from 45° (Golmohammadi et al., 2021).

3. Results and discussion

3.1. Fluid displacement in a single junction

Micro-models with simple geometries have been used to understand fluid displacement mechanisms at the pore scale (Lenormand et al., 1983; Zacharoudiou et al., 2017; Wu et al., 2016; Pavuluri et al., 2020; Tsao et al., 2021). Here, we adopt a pore body with square shape, which is connected to four throats of different widths as shown in Fig. 4(A). The outlet is indicated by red lines. During the drainage process (intrinsic contact angle $\theta_0 = 150°$), the invading fluid fills the pore first before advancing to the widest throat. Trapping of the defending phase at corners is also observed within the pore-body (see Movie S1). These observations are consistent with past experiments (Lenormand et al., 1983; Zacharoudiou et al., 2017). For imbibition, we consider three scenarios with one, two, or three inlets, which will be referred to as I_1, I_2, and I_3 imbibition, respectively. During I_1 imbibition (Movie S2), the invading phase partially fills the pore body, implying that it does not have access to all throats that are connected to the pore. As shown in Fig. 4(A), the invading phase eventually advances towards the left throat as the narrowest throat (top throat) is inaccessible to the invading fluid throughout the displacement process. This limited

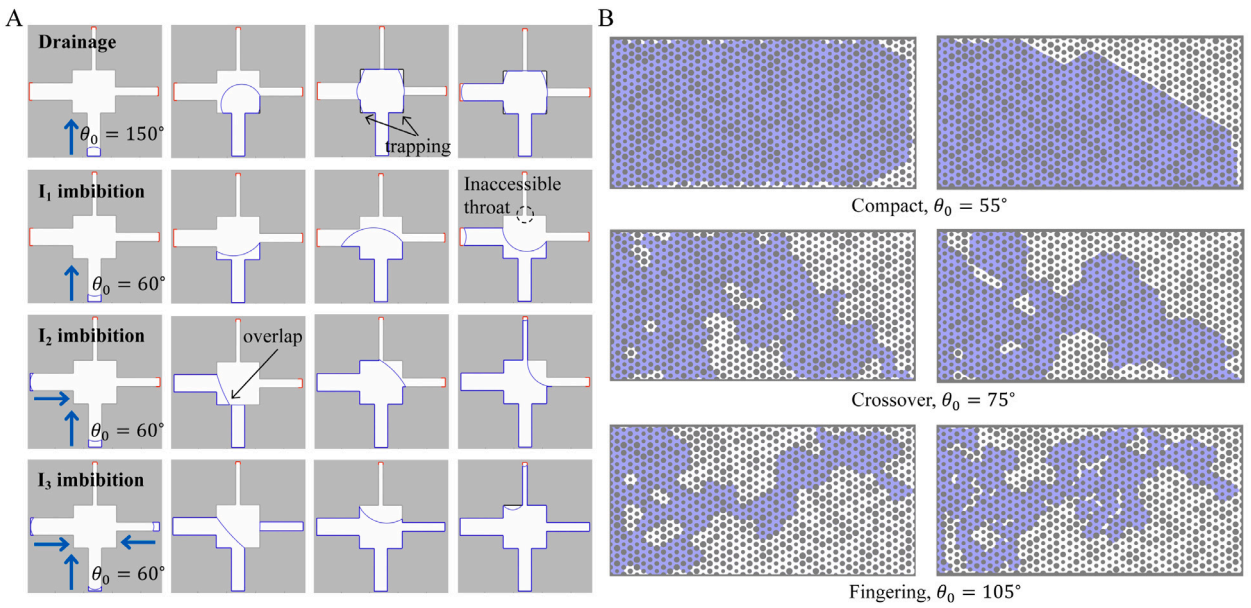

Fig. 4. Validation of the interface tracking algorithm. (A) Two-phase flow in a single square junction for drainage case (top row, $\theta_0 = 150°$) and imbibition (bottom three rows, $\theta_0 = 60°$). Red lines represent outlet. The simulation stops when the invading fluid reaches an outlet. (B) Two-phase flow in disordered porous media with circular grains. The invading phase is injected from the left boundary, with top and bottom boundaries treated as impermeable walls. The left column is the result from Hu et al. (2019), and the right column is from the present algorithm.

accessibility to throats during imbibition process was also identified previously (Blunt, 2017). These observations demonstrate the need to take into account the pore shape for correctly predicting invasion paths. Only considering sizes of pores and throats, as often done in conventional pore filling rules, is insufficient for prediction of the correct invasion paths (Pavuluri et al., 2020). During I_2 imbibition (Movie S3), the fluid in smaller throat moves first due to a smaller capillary pressure until it gets pinned at the sharp corner. Then the invading fluid from the other throat advances. However, the unpin event takes place first at the widest throat. This is due to the concave–convex transition (effective contact angle $\theta < 90°$ within the tube, but $\theta > 90°$ at the sharp corner due to the pinning effect) of the meniscus shape, i.e., the larger throat offers a smaller capillary pressure resistance for the unpin event. Then, the overlap, or cooperative pore filling event (Cieplak and Robbins, 1988; Holtzman and Segre, 2015), takes place and the invading phase moves upwards once it touches the top throat. For I_3 imbibition (Movie S4), an asymmetrical sequence of throat-filling and unpin events is observed again, i.e., throat-filling in smaller throat occurs first while the unpin event happens in the larger throat first. Moreover, it is observed that a snap-off trapping event takes place before the invading phase advances into the top throat. Similar entrapment phenomenon has also been observed in a recent study during the imbibition process (Tsao et al., 2021). In summary, our results of drainage and different types of imbibition processes in a single junction demonstrate the capability of the current algorithm to fully resolve the combined impact of wettability and geometry at the pore scale. This is attributed to the implementation of different types of invasion mechanisms especially the sharp edge pinning phenomenon associated with the unpin event. Some recent studies have highlighted the importance of considering this mechanism using different names, such as "capillary valve effect" in Wu et al. (2016), and "capillary barrier" in Pavuluri et al. (2020).

3.2. Fluid displacement in circle packing

Fig. 4(B) shows the invasion morphology at percolation in disordered porous media with $\theta_0 = \{55°, 75°, 105°\}$. The left columns in Fig. 4(B) are from Hu et al. (2019) using the conventional interface tracking algorithm (Cieplak and Robbins, 1988) assuming perfect spheres, and the right columns are results from the current algorithm. Despite potential uncertainties during image processing and discretization, the transition of invasion morphology in compact, crossover, and fingering regimes is captured faithfully, and the shape of the overall invasion morphology in the original work is reproduced.

3.3. Fluid displacement in realistic porous media

Fig. 5(A) shows the pore structure generated based on a thin section of Berea sandstone (Guo and Aryana, 2019; Alaskar, 2013). Clearly, irregular grains with both convex and concave surfaces are present. Fig. 5(B) shows the color map of the local corner angles (α in Fig. 1(A)) of a sub-region enclosed by the red-box in Fig. 5(A). The corner angle encompasses the geometrical information of the local surface feature, which directly impacts the local pinning strength (upper bound of effective contact angle) calculated by $\theta_0 + (180° - \alpha)$. Fig. 5(C) shows the distribution of the local corner angles for the entire simulation domain, indicating a wide range of α values with a slight shift below 180°. This indicates the overall concavity of grain shapes in the porous medium. Note that in the case of perfect spheres, one would expect a single value of 180° for the corner angle distribution.

The invasion morphologies of fluid displacement at percolation for different contact angles are shown in Fig. 6(A), which are qualitative demonstrations of the impact of wettability on multiphase flow in porous media (also SI Movie 5–7). As the grains or matrix become less wetting to the invading fluid, the displacement pattern shifts from a relatively compact region and a smooth interface, i.e., stable displacement, to a dendritic pattern with many more trapped regions, i.e., capillary fingering. The proportion of pore-scale instabilities, including *burst*, *touch*, and *overlap* events, during the entire displacement process are reported in Fig. 6(B), with insets showing the schematic of each event. At $\theta_0 \approx 80°$, it is observed that the frequency of *overlap* events starts to decrease with the emergence of *burst* events. This is consistent with the established understanding that the *overlap* events tend to smooth the invasion front, whereas *burst* events are associated with patterns described by the theory of invasion percolation (Wilkinson and Willemsen, 1983; Lenormand and Zarcone, 1985).

To provide quantitative insights into the drastic transitions in displacement patterns observed in Fig. 6(A), we first consider the statistics of pore space filling status. This is characterized by two metrics:

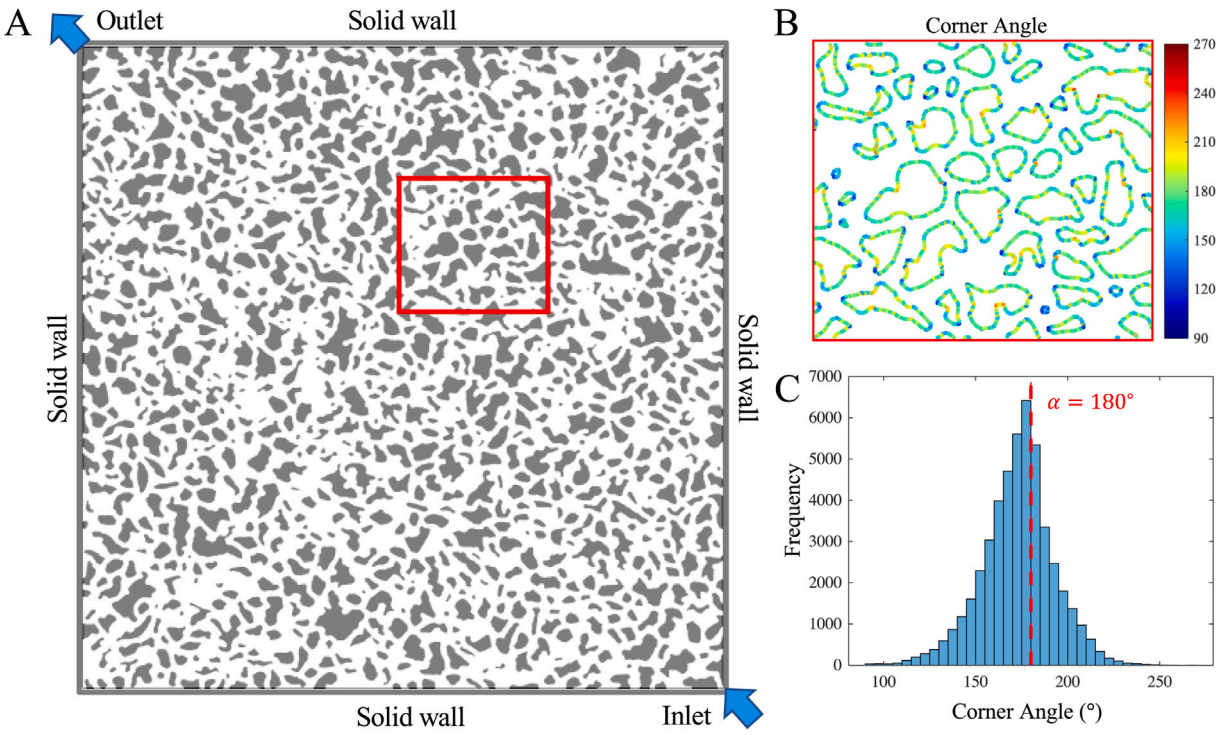

Fig. 5. Porous medium constructed by 2D imaging of Berea sandstone as per Guo and Aryana (2019) (A) Pore geometry with gray and white colors representing grain and pore space, respectively. The point inlet and outlet are located at bottom-right and top-left corners, respectively. The boundaries are solid (impermeable) walls. (B) Corner angle map (α as in Fig. 1(A)) for the sub-region marked by the red box in (A). (C) Corner angle distribution of the whole porous medium. A slight shift below 180° indicates the overall concavity of grain shapes.

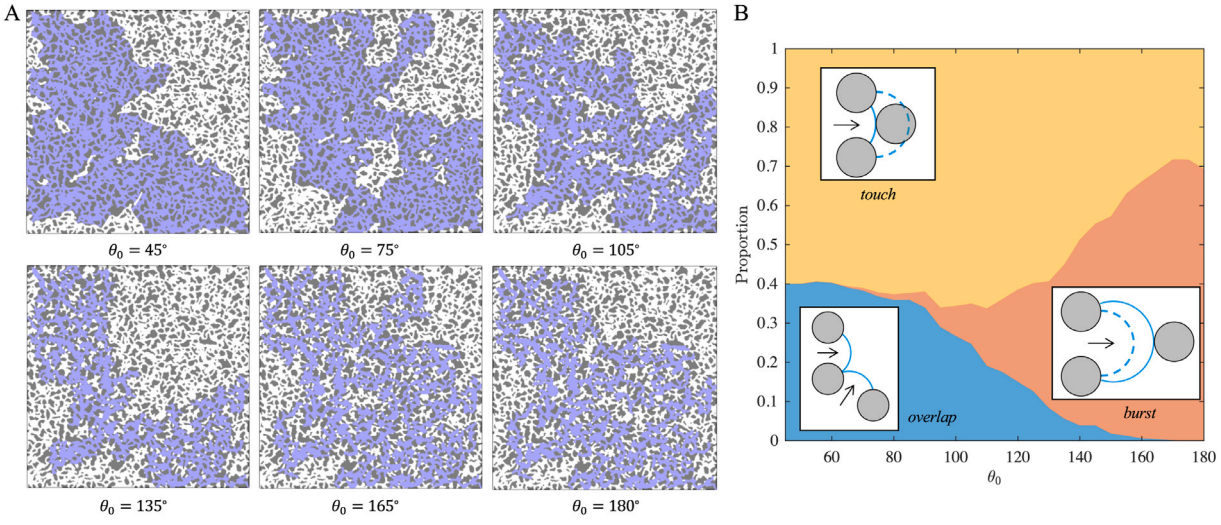

Fig. 6. Fluid–fluid displacement in porous media (A) Final invasion morphologies under different intrinsic contact angles θ_0. (B) Occurrence proportion of pore-scale events as a function of intrinsic contact angle θ_0.

displacement efficiency and fractal dimension. The displacement efficiency, also called the sweep efficiency, measures the proportion of the defending fluid that is displaced out of the porous medium and is of great importance in applications such as oil recovery and carbon sequestration. Fig. 7(A) shows the displacement efficiency across a wide range of contact angles with insets showing the invasion phase in blue color at percolation for $\theta_0 = \{100°, 160°\}$. Despite the general decreasing tendency in displacement efficiency as contact angle θ_0 increases, relatively large fluctuations are observed, implying the significant inherent uncertainties due to heterogeneities in realistic porous media. The huge fluctuations in the relationship between wettability and displacement efficiency are also observed in a recent study using the lattice Boltzmann method (Mora et al., 2021). The fractal dimension D_f, on the other hand, from the theoretical perspective provides a multi-scale characterization of space filling. Fractal dimension values are calculated using the box-counting method (Mandelbrot, 1983) and the results are shown in Fig. 7(B) with the inset showing the box-number vs. box-size in log–log plot for $\theta_0 = 45°$, where the absolute value of the slope is the fractal dimension. It can be seen that D_f decreases from a value of 1.97 to 1.84, corresponding to the regimes of compact displacement and capillary fingering, respectively. These values are consistent with documented values of 1.96 and 1.83 for compact growth and invasion percolation, respectively (Wilkinson and Willemsen, 1983; Lenormand and Zarcone, 1989; Trojer et al., 2015;

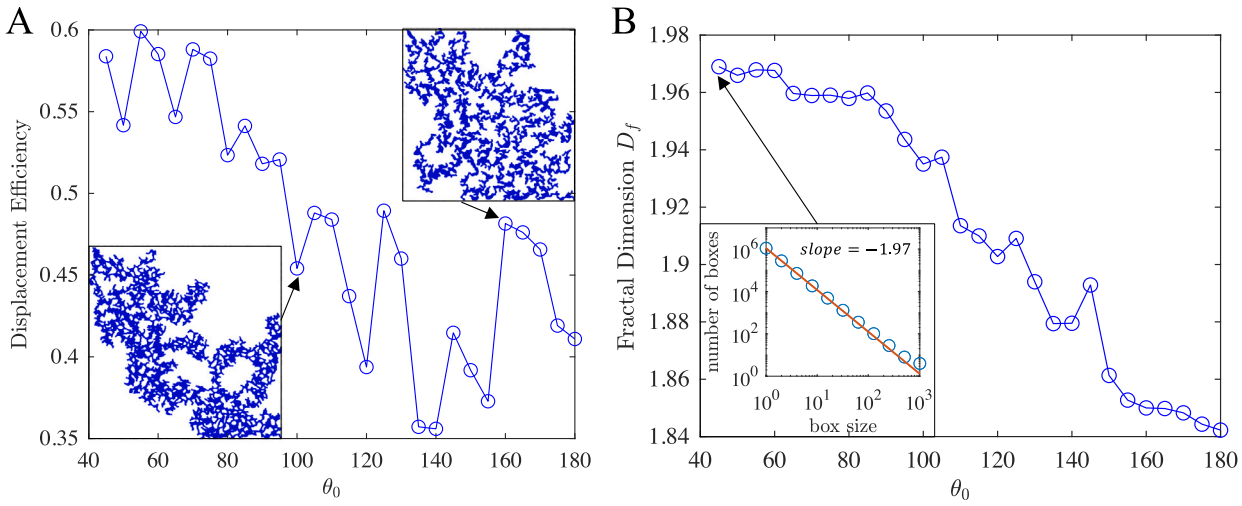

Fig. 7. Characterization of pore filling by the invading fluid. (A) Displacement efficiency, defined as the ratio of displaced defending fluid to the pore space initially occupied by the defending fluid. The insets show two final displacement patterns at $\theta_0 = \{100°, 160°\}$. Only the invading phase is shown. (B) Fractal dimension values for different θ_0 values are calculated using the box-counting method. Inset shows an example of box-number vs. box-size plot for the case $\theta_0 = 45°$.

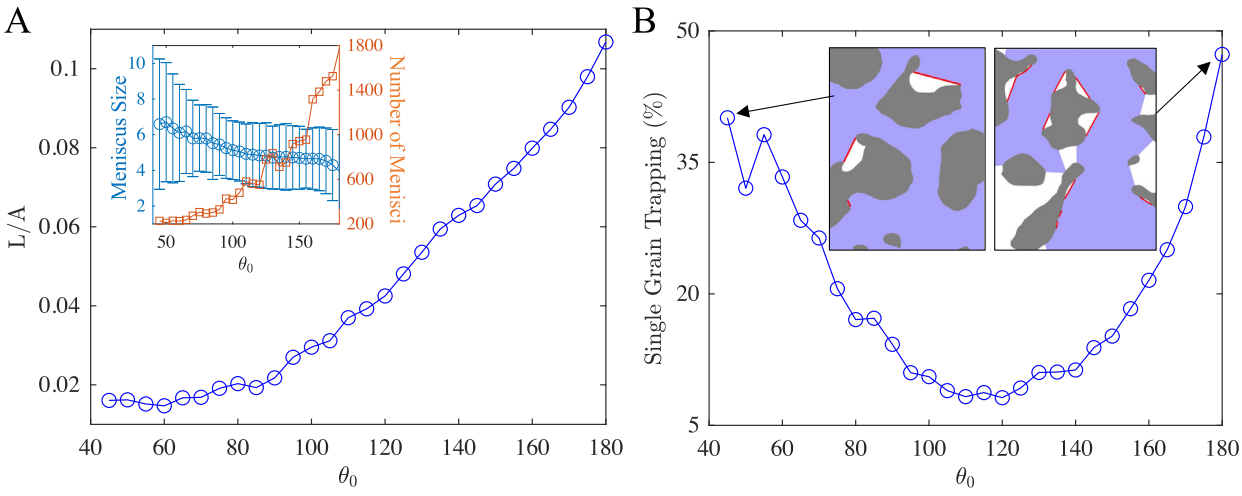

Fig. 8. Fluid–fluid interfacial length. (A) The specific interfacial length of the invading fluid, calculated as the total fluid–fluid interfacial length L divided by the total invaded area A. Inset: left y-axis: average meniscus size (blue circles). Error bars represent standard deviation; right y-axis: number of menisci (red squares) for different θ_0. (B) Percentage of menisci with both of the fluid–fluid–solid triple points belonging to the same grain. Insets show two sub-regions where trapping occurs at $\theta_0 = \{45°, 180°\}$. The single-grain-trapped menisci are marked by red lines. Note that straight lines are drawn here for simplicity.

Zhao et al., 2016; Blunt, 2017; Primkulov et al., 2018). Unlike the sweep efficiency, the fluctuations in D_f become smaller as the contact angle increases, indicating that D_f is less sensitive to the heterogeneity of the porous medium and has stronger a correlation with the wetting condition.

Another key parameter for quantifying immiscible fluid displacement processes is the fluid–fluid interfacial area (length in 2D), which can be of interest for consideration of subsequent chemical reactions between different phases or analysis of interfacial potential energy. Here, we report the specific interfacial length calculated as the ratio of total fluid–fluid interfacial length L divided by the area occupied by the invading phase, A, at percolation. As can be seen in Fig. 8(A), as θ_0 increases, L/A is relatively constant for small values of θ_0 and starts to monotonically increase at $\theta_0 \approx 80°$. The intrinsic contact angle at which L/A starts to increase coincides with the emergence of the *burst* events as in Fig. 6(B). The inset reveals the average (with error bars representing the standard deviation) of meniscus size shown with blue circles and total number of menisci shown with red squares. It can be seen that the average meniscus size decreases, implying the menisci tend to be stuck in narrower throats as θ_0 increases, and the main contributing factor that leads to an overall increase in the specific interfacial length is the increase in the number of menisci. In Fig. 8(B), we show the percentage of menisci that are associated with a single-grain trapping (SGT) where the trapped region can be regarded as being situated within a dead end. This type of trapping is different from the trapped defending phase in the pore body among several grains since it can be much harder to be further mobilized by, for example, momentum transfer when the injection velocity is increased. The insets in Fig. 8(B) show two zoomed-in snapshots of trapped defending phase at imbibition ($\theta_0 = 45°$) and drainage ($\theta_0 = 180°$) conditions with menisci that belong to SGT marked by red lines (the menisci shape is drawn with straight lines for simplicity). As expected, SGT tends to take place at locations where the grain is convex, and the likelihood of the occurrence of SGT in drainage is much greater than in imbibition. Particularly, SGT in drainage can be also thought as the Cassie–Baxter wetting state, where the trapped defending phase in roughness grooves are observed (Cassie and Baxter, 1944; He et al., 2004; Wang et al., 2020). Fig. 8(B) shows a non-monotonic relationship between SGT and θ_0. We note that the occurrence of SGT depends on the geometrical feature of grain shape and the value of contact angle. An investigation

of obstacle shape effect on SGT can be found in Lee et al. (2017). The importance of incorporating SGT phenomenon under drainage condition (by modifying the criterion for overlap event) is examined in Primkulov et al. (2018).

3.4. Discussion

We have presented a pore-resolved interface tracking algorithm for immiscible fluid–fluid displacement simulations. Through discretization of pore space and incorporation of essential pore-scale invasion mechanisms, the method is able to accurately track the interface motion during multiphase flow and reproduce the macroscopic invasion patterns in arbitrarily structured porous media, including reconstructed pore geometries from 2D scans of rock samples. Potential future extensions include adding viscous effects by, for example, using the moving capacitor model (Primkulov et al., 2019). Other modifications for simulating multiphase flow in porous media characterized by heterogeneous wettability, i.e., with spatial variations in intrinsic contact angles, or consideration of gravitational effects by adding height and density dependent values to the critical capillary pressure, can be easily implemented. The present algorithm is highly efficient compared with other conventional computational fluid dynamics methods, e.g., Volume of Fluid (VOF) method or lattice Boltzmann method (LBM) (Ambekar et al., 2021; Wang et al., 2019). Most simulations reported in this work take less than one minute to finish on a laptop.

4. Conclusions

In this work, we present a rigorous interface tracking algorithm for simulating fluid displacement processes under quasi-static conditions. Essential pore-scale meniscus advancement mechanisms, including *burst*, *touch*, *overlap*, *unpin*, and *trapping* have been incorporated. The algorithm is applicable to porous media with arbitrary pore structure for both imbibition and drainage conditions. By conducting multiphase flow simulations on a single junction and disordered porous media, we demonstrate the capability and validity of this algorithm for accurately capturing invasion mechanisms at pore scale and for reproducing the macroscopic invasion morphology.

We then conduct systematic simulations of fluid displacement processes across a wide range of intrinsic contact angles in a realistic porous medium that is a representation of a Berea sandstone. The transition from compact displacement to capillary fingering is demonstrated qualitatively and quantitatively. Important metrics, including displacement efficiency, fractal dimension, and interfacial length, are analyzed. Compared with displacement efficiency, smaller fluctuations are observed in fractal dimension and specific interfacial length, indicating that the latter two metrics are less sensitive to the heterogeneity of the porous medium and have a stronger correlation with the wetting condition of the matrix. This work provides insights into characterization of displacement patterns in porous media and the presented interface tracking algorithm offers an efficient tool for further exploration of effects of wettability, geometry, and topology on multiphase flow in realistic porous materials, which may facilitate the prediction and control of fluid transport phenomena in various engineering applications.

CRediT authorship contribution statement

Zhongzheng Wang: Conceptualization, Methodology, Formal analysis, Writing – original draft. **Jean-Michel Pereira:** Conceptualization, Supervision, Writing – review & editing. **Emilie Sauret:** Resources, Supervision, Writing – review & editing. **Saman A. Aryana:** Resources, Writing – review & editing. **Zhang Shi:** Formal analysis, Writing – review & editing. **Yixiang Gan:** Conceptualization, Supervision, Writing – review & editing.

Declaration of competing interest

The authors declare that they have no known competing financial interests or personal relationships that could have appeared to influence the work reported in this paper.

Acknowledgments

This work was financially supported by Australian Research Council (Projects DP170102886) and The University of Sydney SOAR Fellowship. YG acknowledges the financial support of Labex MMCD (ANR-11-LABX-022-01) for his stay at Laboratoire Navier at ENPC.

Appendix A. Supplementary data

Supplementary material related to this article can be found online at https://doi.org/10.1016/j.advwatres.2022.104152.

References

Alaskar, Mohammed, 2013. In-Situ Multifunctional Nanosensors for Fractured Reservoir Characterization (Ph.D. thesis). Stanford University.
Ambekar, Aniket S., Mondal, Sujoy, Buwa, Vivek V., 2021. Pore-resolved volume-of-fluid simulations of two-phase flow in porous media: Pore-scale flow mechanisms and regime map. Phys. Fluids 33 (10), 102119.
An, Senyou, Erfani, Hamidreza, Godinez-Brizuela, Omar E., Niasar, Vahid, 2020. Transition from viscous fingering to capillary fingering: Application of GPU-based fully implicit dynamic pore network modeling. Water Resour. Res. 56 (12), e2020WR028149.
Armstrong, Ryan T., Georgiadis, Apostolos, Ott, Holger, Klemin, Denis, Berg, Steffen, 2014. Critical capillary number: Desaturation studied with fast X-ray computed microtomography. Geophys. Res. Lett. 41 (1), 55–60.
Bao, Yanyao, Gan, Yixiang, 2020. Roughness effects of gas diffusion layers on droplet dynamics in pemfc flow channels. Int. J. Hydrogen Energy 45 (35), 17869–17881.
Blunt, Martin J., 1998. Physically-based network modeling of multiphase flow in intermediate-wet porous media. J. Pet. Sci. Eng. 20 (3), 117–125.
Blunt, Martin J., 2001. Flow in porous media — pore-network models and multiphase flow. Curr. Opin. Colloid Interface Sci. 6 (3), 197–207.
Blunt, Martin J., 2017. Multiphase Flow in Permeable Media: A Pore-Scale Perspective. Cambridge University Press.
Blunt, Martin, Fayers, F.John, Orr, Franklin M., 1993. Carbon dioxide in enhanced oil recovery. Energy Convers. Manage. 34 (9), 1197–1204, Proceedings of the International Energy Agency Carbon Dioxide Disposal Symposium.
Cassie, A.B.D., Baxter, S., 1944. Wettability of porous surfaces. Trans. Faraday Soc. 40, 546–551.
Cieplak, Marek, Robbins, Mark O., 1988. Dynamical transition in quasistatic fluid invasion in porous media. Phys. Rev. Lett. 60, 2042–2045.
Cieplak, Marek, Robbins, Mark O., 1990. Influence of contact angle on quasistatic fluid invasion of porous media. Phys. Rev. B 41, 11508–11521.
Crisp, D.J., Thorpe, W.H., 1948. The water-protecting properties of insect hairs. Discuss. Faraday Soc. 3, 210–220.
Gibbs, J. Willard, 1961. The Scientific Papers, Vol. 1. Dover Publications, New York.
Golmohammadi, Saeed, Ding, Yi, Küchler, Matthias, Reuter, Danny, Schlüter, Steffen, Amro, Mohd, Geistlinger, Helmut, 2021. Impact of wettability and gravity on fluid displacement and trapping in representative 2D micromodels of porous media (2D sand analogs). Water Resour. Res. 57 (10), e2021WR029908.
Guo, Feng, Aryana, Saman A., 2019. An experimental investigation of flow regimes in imbibition and drainage using a microfluidic platform. Energies 12 (7).
He, Bo, Lee, Junghoon, Patankar, Neelesh A., 2004. Contact angle hysteresis on rough hydrophobic surfaces. Colloids Surf. A 248 (1), 101–104.
Holtzman, R., 2016. Effects of pore-scale disorder on fluid displacement in partially-wettable porous media. Sci. Rep. 6, 36221.
Holtzman, Ran, Segre, Enrico, 2015. Wettability stabilizes fluid invasion into porous media via nonlocal, cooperative pore filling. Phys. Rev. Lett. 115, 164501.
Hu, Ran, Lan, Tian, Wei, Guan-Ju, Chen, Yi-Feng, 2019. Phase diagram of quasi-static immiscible displacement in disordered porous media. J. Fluid Mech. 875, 448–475.
Ju, Yang, Gong, Wenbo, Chang, Wei, Sun, Min, 2020. Effects of pore characteristics on water-oil two-phase displacement in non-homogeneous pore structures: A pore-scale lattice Boltzmann model considering various fluid density ratios. Internat. J. Engrg. Sci. 154, 103343.
Jung, Michael, Brinkmann, Martin, Seemann, Ralf, Hiller, Thomas, Sanchez de La Lama, Marta, Herminghaus, Stephan, 2016. Wettability controls slow immiscible displacement through local interfacial instabilities. Phys. Rev. Fluids 1, 074202.
Lake, Larry W., Johns, Russell, Rossen, Bill, Pope, Gary, 2014. Fundamentals of Enhanced Oil Recovery. Society of Petroleum Engineers.

Lee, Hyundo, Gupta, Ankur, Hatton, T. Alan, Doyle, Patrick S., 2017. Creating isolated liquid compartments using photopatterned obstacles in microfluidics. Phys. Rev. Appl. 7, 044013.
Lenormand, R., 1990. Liquids in porous media. J. Phys.: Condens. Matter 2 (S), SA79–SA88.
Lenormand, Roland, Touboul, Eric, Zarcone, Cesar, 1988. Numerical models and experiments on immiscible displacements in porous media. J. Fluid Mech. 189 (165–187).
Lenormand, Roland, Zarcone, Cesar, 1984. Role of roughness and edges during imbibition in square capillaries. In: SPE Annual Technical Conference and Exhibition, vol. All Days.
Lenormand, Roland, Zarcone, Cesar, 1985. Invasion percolation in an etched network: Measurement of a fractal dimension. Phys. Rev. Lett. 54, 2226–2229.
Lenormand, Roland, Zarcone, Cesar, 1989. Capillary fingering: Percolation and fractal dimension. Transp. Porous Media 4 (6), 599–612.
Lenormand, R., Zarcone, C., Sarr, A., 1983. Mechanisms of the displacement of one fluid by another in a network of capillary ducts. J. Fluid Mech. 135, 337–353.
Lipiec, J., Kuś, J., Słowińska-Jurkiewicz, A., Nosalewicz, A., 2006. Soil porosity and water infiltration as influenced by tillage methods. Soil Tillage Res. 89 (2), 210–220.
Mandelbrot, B.B., 1983. The Fractal Geometry of Nature, third ed. W. H. Freeman and Comp., New York.
Mason, Geoffrey, Morrow, Norman R., 1994. Effect of contact angle on capillary displacement curvatures in pore throats formed by spheres. J. Colloid Interface Sci. 168 (1), 130–141.
Matter, Juerg M., Stute, Martin, Snæbjörnsdottir, Sandra Ó., Oelkers, Eric H., Gislason, Sigurdur R., Aradottir, Edda S., Sigfusson, Bergur, Gunnarsson, Ingvi, Sigurdardottir, Holmfridur, Gunnlaugsson, Einar, Axelsson, Gudni, Alfredsson, Helgi A., Wolff-Boenisch, Domenik, Mesfin, Kiflom, Taya, Diana Fernandez de la Reguera, Hall, Jennifer, Dideriksen, Knud, Broecker, Wallace S., 2016. Rapid carbon mineralization for permanent disposal of anthropogenic carbon dioxide emissions. Science 352 (6291), 1312–1314.
Mora, Peter, Morra, Gabriele, Yuen, Dave A., Juanes, Ruben, 2021. Influence of wetting on viscous fingering via 2D lattice Boltzmann simulations. Transp. Porous Media 138 (3), 511–538.
Oliver, J.F., Huh, C., Mason, S.G., 1977. Resistance to spreading of liquids by sharp edges. J. Colloid Interface Sci. 59 (3), 568–581.
Paterson, Lincoln, 1984. Diffusion-limited aggregation and two-fluid displacements in porous media. Phys. Rev. Lett. 52, 1621–1624.
Patmonoaji, Aninditiyo, Muharrik, Mushlih, Hu, Yingxue, Zhang, Chunwei, Suekane, Tetsuya, 2020. Three-dimensional fingering structures in immiscible flow at the crossover from viscous to capillary fingering. Int. J. Multiph. Flow. 122, 103147.
Pavuluri, Saideep, Maes, Julien, Yang, Jianhui, Regaieg, Mohamed, Moncorgé, Arthur, Doster, Florian, 2020. Towards pore network modelling of spontaneous imbibition: contact angle dependent invasion patterns and the occurrence of dynamic capillary barriers. Comput. Geosci. 24 (2), 951–969.
Primkulov, Bauyrzhan K., Pahlavan, Amir A., Fu, Xiaojing, Zhao, Benzhong, MacMinn, Christopher W., Juanes, Ruben, 2019. Signatures of fluid–fluid displacement in porous media: wettability, patterns and pressures. J. Fluid Mech. 875, R4.
Primkulov, Bauyrzhan K., Talman, Stephen, Khaleghi, Keivan, Rangriz Shokri, Alireza, Chalaturnyk, Rick, Zhao, Benzhong, MacMinn, Christopher W., Juanes, Ruben, 2018. Quasistatic fluid-fluid displacement in porous media: Invasion-percolation through a wetting transition. Phys. Rev. Fluids 3, 104001.
Purcell, W.R., 1950. Interpretation of capillary pressure data. J. Pet. Technol. 2 (08), 11–12.
Ran, Hu, Jiamin, Wan, Zhibing, Yang, Yi-Feng, Chen, Tetsu, Tokunaga, 2018. Wettability and flow rate impacts on immiscible displacement: A theoretical model. Geophys. Res. Lett. 45 (7), 3077–3086.
Shi, Zhang, Wang, Zhongzheng, Gan, Yixiang, 2021. Effects of topological disorder in unsaturated granular media via a pore-scale lattice Boltzmann investigation. Adv. Water Resour. 149, 103855.
Singh, Kamaljit, Scholl, Hagen, Brinkmann, Martin, Michiel, Marco Di, Scheel, Mario, Herminghaus, Stephan, Seemann, Ralf, 2017. The role of local instabilities in fluid invasion into permeable media. Sci. Rep. 7 (1), 444.
Szulczewski, Michael L., MacMinn, Christopher W., Herzog, Howard J., Juanes, Ruben, 2012. Lifetime of carbon capture and storage as a climate-change mitigation technology. Proc. Natl. Acad. Sci. 109 (14), 5185–5189.
Trojer, Mathias, Szulczewski, Michael L., Juanes, Ruben, 2015. Stabilizing fluid-fluid displacements in porous media through wettability alteration. Phys. Rev. Appl. 3, 054008.
Tsao, Chia-Wen, Huang, Qun-Zhan, You, Chang-Ye, Hilpert, Markus, Hsu, Shao-Yiu, Lamorski, Krzysztof, Chang, Liang-Cheng, Sławiński, Cezary, 2021. The effect of channel aspect ratio on air entrapment during imbibition in soil-on-a-chip micromodels with 2D and 2.5D pore structures. Lab Chip 21, 385–396.
Wang, Zhongzheng, Chauhan, Kapil, Pereira, Jean-Michel, Gan, Yixiang, 2019. Disorder characterization of porous media and its effect on fluid displacement. Phys. Rev. Fluids 4, 034305.
Wang, Zhongzheng, Pereira, Jean-Michel, Gan, Yixiang, 2020. Effect of wetting transition during multiphase displacement in porous media. Langmuir 36 (9), 2449–2458, PMID: 32070092.
Wang, Zhongzheng, Pereira, Jean-Michel, Gan, Yixiang, 2021. Effect of grain shape on quasi-static fluid-fluid displacement in porous media. Water Resour. Res. 57 (4), e2020WR029415.
Wilkinson, D., Willemsen, J.F., 1983. Invasion percolation: a new form of percolation theory. J. Phys. A: Math. Gen. 16 (14), 3365–3376.
Wu, Rui, Kharaghani, Abdolreza, Tsotsas, Evangelos, 2016. Two-phase flow with capillary valve effect in porous media. Chem. Eng. Sci. 139, 241–248.
Yortsos, Y.C., Xu, B., Salin, D., 1997. Phase diagram of fully developed drainage in porous media. Phys. Rev. Lett. 79, 4581–4584.
Zacharoudiou, Ioannis, Chapman, Emily M., Boek, Edo S., Crawshaw, John P., 2017. Pore-filling events in single junction micro-models with corresponding lattice Boltzmann simulations. J. Fluid Mech. 824, 550–573.
Zhao, Benzhong, MacMinn, Christopher W., Juanes, Ruben, 2016. Wettability control on multiphase flow in patterned microfluidics. Proc. Natl. Acad. Sci. 113 (37), 10251–10256.